ADVANCED FUNCTIONAL MATERIALS
www.afm-journal.de

Curved Nanographene–Graphite Hybrid Anodes with Sequential Li^+ Insertion for Fast-Charging and Long-Life Li-Ion Batteries

Hyunji Cha, Minsung Kang, Seung Hak Oh, Jee Ho Ha, Jeongmi Joo, Dae Hyeon Kwon, Sang Kyu Kwak, Seokhoon Ahn,* and Seok Ju Kang**

Graphite remains the most widely used anode material for lithium-ion batteries (LIBs). However, improvements are essential to meet the demand for high-performance anodes in full-cell configurations. Here, the synergistic electrochemical performance of a curved nanographene–graphite hybrid anode composed of mesocarbon microbeads (MCMB) is investigated, and Cl-substituted contorted hexabenzocoronene (Cl-cHBC), designed to improve the specific capacity, rate capability, and cycling stability. The optimized 1:1 blend forms a homogeneous morphology, in which sphere-like MCMB particles are uniformly embedded within needle-like Cl-cHBC crystals without macrophase separation. This architecture enables sequential Li-ion insertion and leads to a synergistic improvement in the electrochemical performance. In a half-cell, the hybrid anode achieves 100 mAh g^{-1} at 4 A g^{-1}, outperforming the pristine MCMB graphite (≈20 mAh g^{-1} at 4 A g^{-1}). In full-cells paired with a single-crystal $LiNi_{1-y-z}Co_yMn_zO_2$811 cathode, it shows exceptional rate capability (≈100 mAh g^{-1} at 5 C) and stability (70% capacity retention after 1000 cycles at 5 C). Furthermore, a pouch cell incorporating the hybrid anode delivers 115 mAh g^{-1} at 1 C and stable performance over 2100 cycles with a Coulombic efficiency of 99%. These results demonstrate the practical potential of sequential Li-ion insertion into Cl-cHBC/MCMB composites for high-performance LIB applications.

1. Introduction

Graphite is undoubtedly the most successful anode material for secondary Li-ion batteries (LIBs) due to its light weight, high conductivity, cost-effectiveness, satisfactory specific capacity, and high reversibility.[1–7] In particular, its low redox potential, close to 0 V versus Li/Li^+, minimizes the voltage penalty when paired with conventional cathode materials such as $LiFePO_4$ (LFP), $LiCoO_2$ (LCO), and Ni-rich $LiNi_{1-y-z}Co_yMn_zO_2$ (NCM), and secures 98% of the market share for anode materials.[8] Despite this dominance, ongoing efforts are aimed at improving graphite anodes to meet high-energy density, high-rate capability, and low-temperature operation requirements of LIBs to ensure continued market viability.[9–11] A notable development in graphite-based anodes for the current LIB industry is the integration of Si into graphite.[12–16] The remarkably high theoretical capacity of Si (3578 mAh g^{-1}), resulting from the Li-Si alloy, provides an effective way to increase the energy density of LIBs.[17–21] For instance, a graphite-Si composite anode with only 8% Si significantly improves the specific capacity while minimizing the large volume changes typically observed in pure Si anodes.[22] In addition, the low redox potential of ≈0.5 V versus Li/Li^+ mitigates the formation of Li metal on the anode surface.[12] However, graphite-Si composite anodes still face the problem of unsatisfactory rate capability and cycling performance, which necessitates further improvements in their electrochemical behavior in full-cell configurations.

H. Cha, S. H. Oh, J. H. Ha, J. Joo, S. J. Kang
School of Energy and Chemical Engineering
Ulsan National Institute of Science and Technology (UNIST)
Ulsan 44919, Republic of Korea
E-mail: sjkang@unist.ac.kr

The ORCID identification number(s) for the author(s) of this article can be found under https://doi.org/10.1002/adfm.202514795

DOI: 10.1002/adfm.202514795

M. Kang, S. Ahn
Institute of Advanced Composite Materials
Korea Institute of Science and Technology
Jeonbuk 55324, Republic of Korea
E-mail: ahn75@kist.re.kr

D. H. Kwon, S. K. Kwak
Department of Chemical and Biological Engineering
Korea University
Seoul 02841, Republic of Korea
E-mail: skkwak@korea.ac.kr

Recently, small organic molecules have attracted interest as anode materials mainly due to their cost-effectiveness, ease of synthesis, and tunability.[23–29] Among the proposed anode materials, highly crystalline curved nanographenes, such as contorted hexabenzocoronene (cHBC), which belongs to the polyaromatic hydrocarbon family, offer remarkable stability in conventional organic electrolytes, effectively mitigating the dissolution problems commonly observed with other organic materials.[30–36] In particular, the superior rate performance of the cHBC anode, compared to conventional graphite, is attributed to its large interspacing of 4.6 Å and short diffusion length, making it a promising candidate for high-performance organic anodes.[30] Moreover, the Li storage characteristics of cHBC can be easily customized by simply halogenating peripheral aromatic rings with elements such as fluorine (F) or chlorine (Cl).[31,34,36] Thus, fluorinated cHBC anodes exhibit pseudocapacitive behavior and achieve specific capacities of ≈100 mAh g^{-1} even at high current densities of 7 A g^{-1}.[31] Similarly, the Cl-cHBC anode shows impressive rate performance, attributed to its eclipsed AA stacking and strong Cl–Cl interactions, leading to large intercolumnar spacings (≈15 Å).[34,36] In addition to their high-rate performance, Cl-cHBC anodes deliver promising electrochemical performance in full-cell configurations when paired with conventional LFP, LCO, and single-crystal NCM811 cathodes, highlighting their potential as a high-performance anode material.[36]

Despite the promising electrochemical properties of cHBC and its halogenated derivatives, their practical application as standalone anode materials in commercial LIBs is limited due to several inherent drawbacks, such as low electrical conductivity, low tap density, and moderate specific capacity.[30–34,36,37] To overcome these challenges and improve the practicality of cHBC-based anodes, combining them with conventional graphite could provide a practical solution by simultaneously leveraging the high-rate and long cycle life, and improving the conductivity, tap density, and specific capacities. Although several approaches for composite or hybrid anodes incorporating graphite have been investigated recently to address these limitations, many of these strategies rely on complex synthetic protocols involving multistep chemical reactions,[38,39] high-temperature annealing,[40,41] elaborate surface modifications,[11,42] the use of toxic solvents[13] or time-consuming processing procedure,[43] which ultimately hinders scalability. As summarized in Table S1 (Supporting Information), representative hybrid graphite anodes reported in the literature exhibit a wide range of electrochemical performance, with specific capacities ranging from ≈160 to over 1500 mAh g^{-1}, rate capabilities of over 200 mAh g^{-1} even at high current densities, and cycling stabilities of several hundred to thousands of cycles. However, this performance is usually achieved through the complex processes mentioned above, often in combination with toxic reagents or tightly controlled surface modifications, which substantially limit large-scale implementation. Structure–property analyses further indicate that strategies such as morphological confinement, interfacial engineering, or the integration of conductive networks can improve Li ion transport and mechanical stability; however, these approaches inevitably lead to considerable complexity in fabrication. For large-scale production, a simple and scalable mechanical mixing strategy is highly desirable due to its operational simplicity and compatibility with existing electrode manufacturing infrastructure. Nevertheless, the currently known mechanically blended systems often require additional processing steps to ensure homogeneity or rely on high-temperature conditions and sophisticated synthesis techniques that are impractical for industrial applications.[44–47] Therefore, the rational design of graphite-based hybrid anodes with optimized morphologies and synergies remains a key challenge for the realization of practical high-performance LIB anodes.

In this study, we explore a curved nanographene–graphite hybrid anode consisting of conventional MCMB and Cl-cHBC, engineered to enable sequential Li^+ insertion for fast-charging and long-life LIBs. When the blend ratio is optimized to 1:1, the composite forms a smooth, homogeneous morphology in which sphere-like MCMB particles are uniformly embedded within the needle-like Cl-cHBC crystals without phase separation. This unique microstructure takes advantage of both components: the large interlayer spacing, high rate capability, and structural stability of Cl-cHBC and the excellent electrical conductivity and specific capacity of MCMB. Monte Carlo (MC) simulations combined with density functional theory (DFT) calculations reveal a sequential Li insertion process within the composite, demonstrating how the distinctive crystal structure enables excellent electrochemical behavior. Electrochemical tests in a half-cell configuration support these findings. The hybrid anode delivers a specific capacity of 100 mAh g^{-1} at a high current density of 4 A g^{-1}, clearly outperforming pristine MCMB graphite (≈20 mAh g^{-1} at 4 A g^{-1}). When combined with a single-crystal NCM811 cathode, the hybrid anode also demonstrated outstanding rate capability (100 mAh g^{-1} at 5 C) and excellent cycling stability, retaining 70% of its capacity after 1000 cycles at 5 C without significant degradation. In addition to the coin cell-scale evaluations, the practical applicability of the hybrid anode is further validated in a pouch cell configuration. A high specific capacity of ≈115 mAh g^{-1} at 1 C is achieved, and stable operation is maintained over 2100 cycles with a Coulombic efficiency of 99%. These results suggest the potential of graphite–curved nanographene hybrid anodes as a promising strategy for the development of high-performance LIBs.

2. Results and Discussion

2.1. Synergistic Effect of Curved Nanographene-Graphite Hybrid Anode

To achieve a synergistic effect between the highly crystalline curved nanographene and the conventional graphite (Figure S1, Supporting Information), the ratio to fabricate a hybrid anode was systematically varied, as schematically shown in **Figure 1**. The goal of this composite design was to leverage the complementary strengths of both materials to improve the overall electrochemical performance. Notable advantages of cHBC and its derivatives include a high rate capability, large *d*-spacing, ease of synthesis, and the ability to reduce Li metal deposition. In particular, the large *d*-spacing and short diffusion length are key features that facilitate efficient Li-ion access during the intercalation and deintercalation processes.[30,34,36] However, despite these advantages, Cl-cHBC suffers from inherently low electrical conductivity and moderate gravimetric and

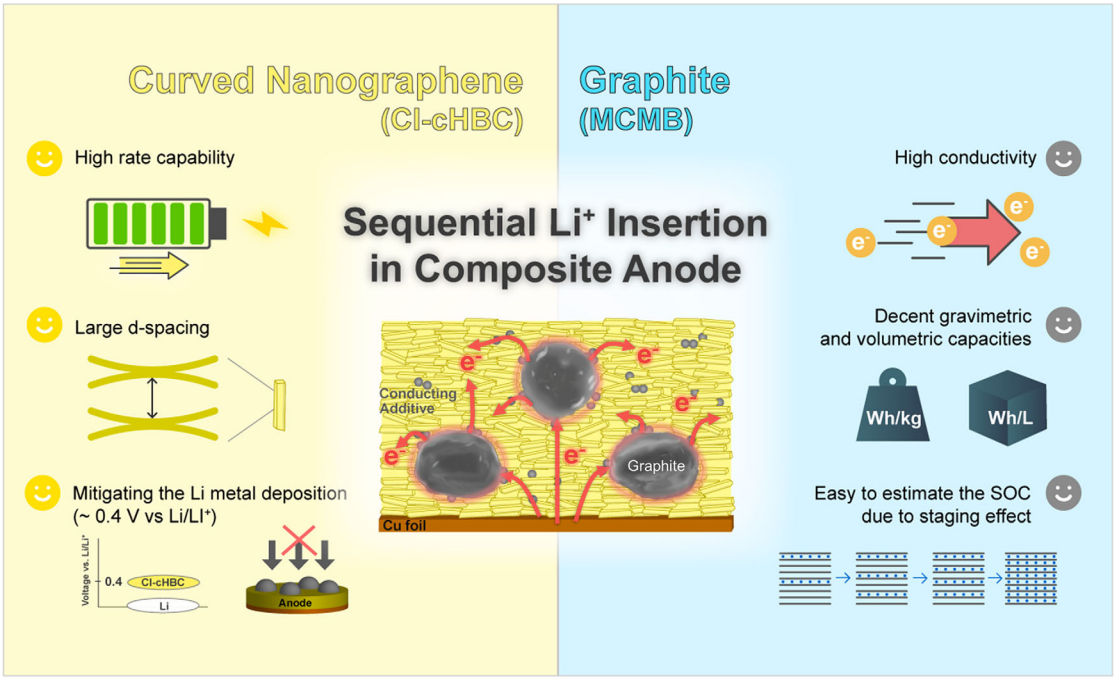

Figure 1. Schematic representation of the synergistic effect between Cl-cHBC and MCMB graphite in the hybrid anode.

volumetric capacities, which limit its standalone application. In contrast, conventional graphite anodes have high electrical conductivities and favorable gravimetric and volumetric capacities, making them the current industry standard.[48] Nevertheless, their relatively low rate performances, stemming from their narrow *d*-spacing and long diffusion paths, hinder their effectiveness as high-performance battery anodes.[49] Furthermore, the low redox potential of graphite increases the risk of Li metal deposition, especially at high current densities, raising significant safety concerns.[50] Given these complementary yet contrasting properties, the blending of curved nanographene and graphite in an optimized ratio offers a promising strategy to overcome the individual limitations of each material. The resulting hybrid anode effectively combined the structural and kinetic advantages of Cl-cHBC with the excellent conductivity and capacity of graphite. This synergistic combination not only improves the overall electrochemical performance but also mitigates issues such as Li metal deposition, providing greater safety and durability in practical LIB applications.

2.2. Morphologies of Curved Nanographene-Graphite Hybrid Anodes

The morphologies of Cl-cHBC and MCMB graphite hybrid anodes were investigated by scanning electron microscopy (SEM) to observe the structural integration of the two components. A series of hybrid anodes was prepared by mixing Cl-cHBC and conventional MCMB graphite in varying ratios from 1:0 to 0:1, with 10 wt.% PVDF binder and 10 wt.% conducting agent. The resulting slurries were coated onto Cu current collectors and then thermally annealed in a vacuum oven at 120 °C to remove the residual NMP solvent and enhance the crystallinity of Cl-cHBC.[34,36] To further improve the crystallinity of the hybrid anodes, the dried electrodes were annealed at 330 °C for 50 min under an argon atmosphere. X-ray diffraction (XRD) analysis of Cl-cHBC, MCMB graphite, and their 1:1 hybrid electrodes revealed sharper diffraction peaks with a lower full-width half-maximum (FWHM), confirming improved crystallinity after thermal annealing (Figure S2, Supporting Information). In addition, Raman spectroscopy was performed on pristine Cl-cHBC (1064 nm excitation) and the 1:1 hybrid anode (325 m excitation) before and after annealing. Well-preserved Raman characteristic peaks were observed, indicating that the thermal annealing did not substantially alter the molecular structure (Figure S3, Supporting Information). Of note, the applied annealing temperature of 330 °C was insufficient to induce the graphitization of the Cl-cHBC, a process that normally requires a much higher temperature.[51] As shown in **Figure 2a**, the pristine Cl-cHBC electrode exhibits a distinct needle-like morphology, indicating its high crystallinity, and consistent with previous reports.[34,36] We also observed the pristine MCMB graphite surface, which exhibited the typical sphere-like MCMB morphology with an average diameter of ≈10–20 µm (Figure 2e).[52] The hybrid anodes with Cl-cHBC:MCMB graphite ratios of 3:1, 1:1, and 1:3 exhibited a homogeneous blend of the two materials without macrophase separation (Figure 2b–d; Figure S2, Supporting Information). Moreover, the corresponding EDX elemental mapping of Cl showed that the presence of sphere-like MCMB morphology decreases with increasing Cl-cHBC region as the ratio shifts from 1:3 to 3:1. To gain further insight into the internal structure, a cross-sectional SEM examination was performed using the ion milling method. In agreement

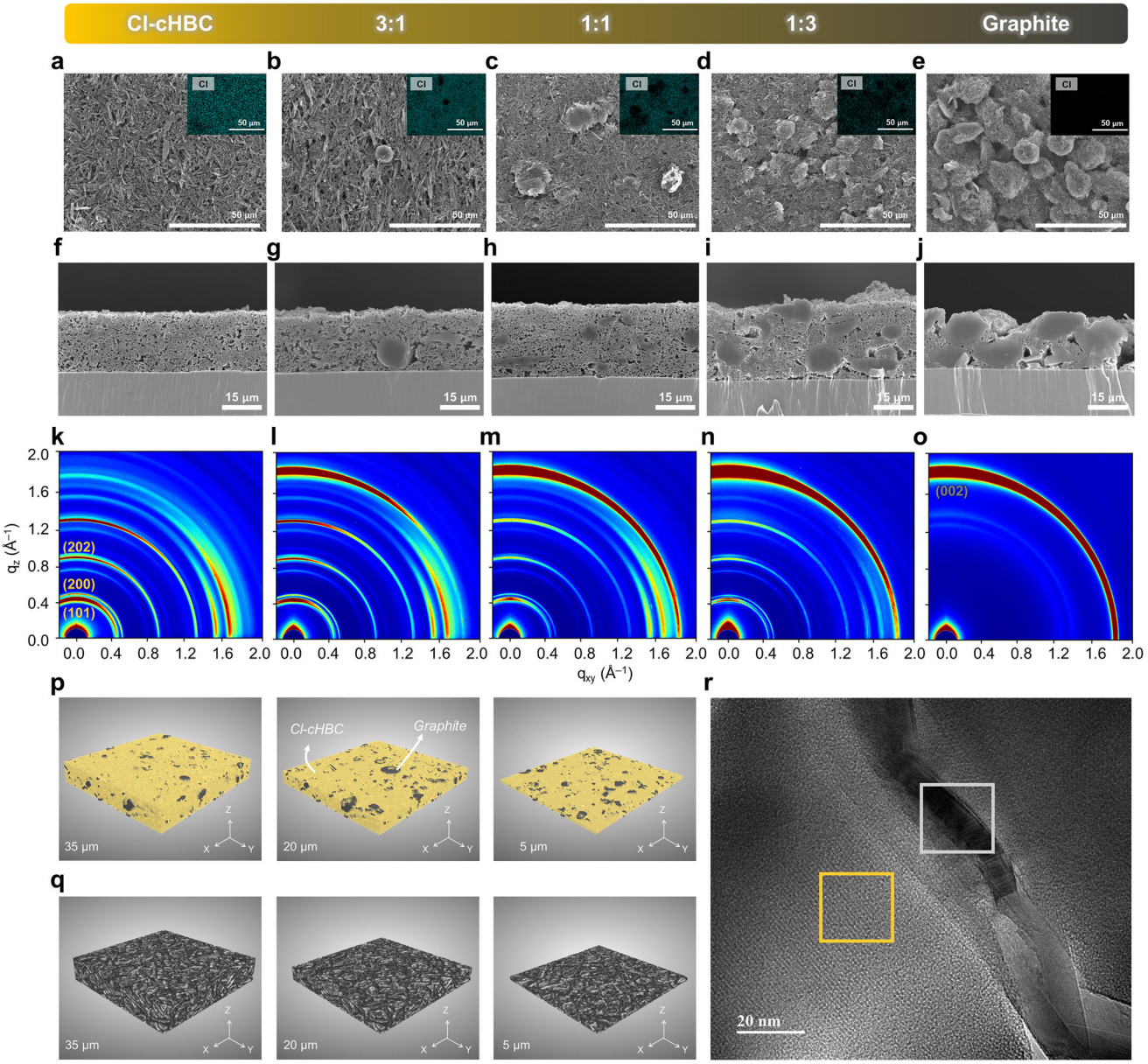

Figure 2. Plane and cross-sectional SEM images of a,f) pristine Cl-cHBC, b,g) 3:1, c,h) 1:1, d,i) 1:3, and e,j) pristine MCMB graphite anodes. The insets in a–e) show the corresponding EDX elemental mapping of Cl. 2D-GIWAXS patterns of k) pristine Cl-cHBC, l) 3:1, m) 1:1, n) 1:3, and o) pristine MCMB graphite anodes. Depth-resolved XRM images of p) 1:1 and q) pristine MCMB graphite anodes. r) Cross-sectional bright-field TEM image of the 1:1 hybrid anode, where the yellow and gray rectangular regions represent Cl-cHBC and graphite, respectively.

with the top-view SEM images, the cross-sectional SEM images confirmed the uniform distribution of the sphere-like MCMB particles embedded within the Cl-cHBC crystal matrix at all composite ratios (Figure 2f–j; Figure S4, Supporting Information). It is noteworthy that the relative population of Cl-cHBC decreased with increasing MCMB content. In addition, the surface roughness becomes more pronounced at higher MCMB ratios, as is evident from the cross-sectional and tilted SEM images (Figures S5 and S6, Supporting Information). This roughness is attributed to the large sphere-like MCMB particles (≈15 μm), which cause uneven pressure distribution during the roll-pressing process, and form a rough surface topology. In contrast, the electrodes with a higher proportion of Cl-cHBC crystals exhibited much smoother surfaces during compression as they were able to conform and compact more uniformly. The interplay between Cl-cHBC and MCMB graphite within the hybrid anode, therefore, not only enables a homogeneous morphology but also contributes to a smoother electrode surface. This effectively reduces the formation of rough surface topologies, which are typically associated with a high MCMB content, and the current can be uniformly distributed over the electrode surface.

2.3. GIWAXS Analysis of Curved Nanographene-Graphite Hybrid Anodes

The crystal structures of the hybrid electrodes were examined using 2D grazing-incidence wide-angle X-ray diffraction scattering (GIWAXS) analysis.[53] The use of a high-flux synchrotron beam allowed the capture of the diffraction patterns of both Cl-cHBC and MCMB within the composite structure. The pristine Cl-cHBC anode exhibited sharp and well-defined diffraction peaks at q = 0.46 and q = 0.93 Å, corresponding to the (101) and (202) planes, respectively, which are in good agreement with previous reports (Figure 2k).[34] The high crystallinity of Cl-cHBC is further supported by the narrow FWHM observed in the corresponding 1D diffraction pattern (Figure S7, Supporting Information). This high degree of crystallinity is primarily attributed to the previously applied anti-solvent treatment method, which effectively improves both the structural order and electrochemical performance of Cl-cHBC.[36] Similarly, the pristine MCMB graphite anode exhibited a strong Bragg reflection at q = 1.87 Å, which corresponds to the (002) plane of graphite with a d-spacing of 0.335 nm (Figure 2o; Figure S7, Supporting Information).[54,55] GIWAXS analysis also provided clear insights into the crystal structure of the hybrid anodes. The hybrid anodes with Cl-cHBC: MCMB graphite ratios of 3:1, 1:1, and 1:3 showed combined diffraction patterns, displaying distinct peaks at q = 0.46, 0.93, and 1.87 Å. This confirms the coexistence of both Cl-cHBC and MCMB graphite phases within the hybrid anodes. Furthermore, the 1D diffraction pattern revealed a clear correlation between the peak intensities and the blend ratio (Figure S7, Supporting Information). Specifically, the intensities of the Cl-cHBC peaks systematically decreased when the proportion of MCMB graphite increased, whereas the intensity of the graphite peak increased accordingly. These structural findings indicate that the hybrid anode retained the crystallinity of both Cl-cHBC and MCMB graphite across all blending ratios, supporting the stable coexistence and uniform distribution of the two components.

2.4. Multiscale Structural Analysis of 1:1 Hybrid Anodes

To further elucidate the structural advantages of the 1:1 hybrid anode, its internal morphology was examined using 3D X-ray microscopy (XRM). The resulting XRM images revealed a homogeneously dispersed distribution of sphere-like MCMB graphite particles embedded within the needle-like Cl-cHBC matrix throughout the depth of the electrode (Figure 2p; Video S1, Supporting Information). This well-integrated structure provided continuous and efficient electrical pathways within the hybrid anode, which enabled uniform electron transport and maximized the electrochemical activation of Cl-cHBC during battery operation. In contrast, the pristine MCMB graphite anode exhibited a significantly different morphology. XRM analysis revealed the presence of large, loosely packed sphere-like MCMB graphite particles, which led to the formation of an uneven electrode interface and the development of a rough surface texture (Figure 2q; Video S2, Supporting Information). Quantitative pore analysis further supported this structural deficiency. The pristine MCMB graphite anode exhibited a high pore-to-total volume ratio, which contributed to substantial dead volume and reduced the packing density, ultimately limiting the achievable volumetric energy density (Table S4, Supporting Information). In comparison, the 1:1 hybrid anode exhibited a significantly lower pore volume ratio, which contributed to a more uniform pressure distribution during the roll-pressing process, resulting in a smoother and denser electrode structure and higher volumetric energy density. In particular, the tap density of the 1:1 hybrid anode was measured (Figure S8a, Supporting Information), which enables a theoretical volumetric capacity of 501 mAh cm^{-3} (Figure S8b, Supporting Information). To gain further insight into the nanoscale structure of the composite, a high-resolution transmission electron microscopy (HR-TEM) of a 1:1 hybrid anode prepared by ultramicrotomy (Figure 2r).[59] The bright-field TEM images confirmed the intimate interfacial contact between the MCMB graphite particles and the Cl-cHBC crystals. In particular, distinct regions corresponding to MCMB graphite and Cl-cHBC were identified, exhibiting characteristic d-spacings of 0.33 nm for MCMB graphite and significantly large intercolumnar spacings of 1.34 nm for Cl-cHBC crystals (Figure S9, Supporting Information).[34,36,54,55] In addition to the structural observations, further extensive physicochemical and mechanical characterizations of the hybrid electrodes were performed, including thermogravimetric analysis and interfacial cutting analysis system measurements, which confirmed their remarkable thermal stability and cohesive strength (Figure S10a,b, Supporting Information). In addition, measurements of the contact angle of the sessile droplets demonstrated the excellent wettability of the surface toward the carbonate electrolyte (Figure S10c, Supporting Information).

2.5. Electrochemical Characteristics of Hybrid Anodes in Half-Cell

The electrochemical characteristics of the hybrid anodes were evaluated in a half-cell configuration, using 1.3 M $LiPF_6$ in ethylene carbonate/diethyl carbonate (EC/DEC, 3:7 v/v) with 10 wt.% fluoroethylene carbonate (FEC) as the electrolyte. As a reference, pristine Cl-cHBC and MCMB graphite anodes were monitored under identical conditions with Li metal as the counter electrode in conventional 2032 coin cells. **Figure 3**a presents the galvanostatic discharge and charge trajectories of the pristine Cl-cHBC anode, which exhibits a single discharge plateau at 0.4 V and delivers a specific capacity of ≈250 mAh g^{-1} at a constant current of 0.1 A g^{-1}, consistent with previous studies.[36] It is worth noting that the specific capacity of Cl-cHBC is limited by its inherently low electrical conductivity. When tested under lower loading (≈0.4 mg cm^{-2}) and reduced current density (0.02 A g^{-1}), the Cl-cHBC electrode achieves an improved specific capacity of 399 mAh g^{-1} (Figure S11, Supporting Information). In comparison, the pristine MCMB graphite anode exhibited characteristic staging behavior and achieved a specific capacity of 350 mAh g^{-1}, which is also in agreement with previous reports.[6] To investigate the synergistic electrochemical effect arising from the combination of Cl-cHBC and MCMB graphite, the discharge and charge behaviors of the hybrid anodes with varying Cl-cHBC:MCMB graphite ratios were studied. The galvanostatic profiles clearly illustrate the relative contributions of the individual components. The capacity contribution of Cl-cHBC (highlighted by the

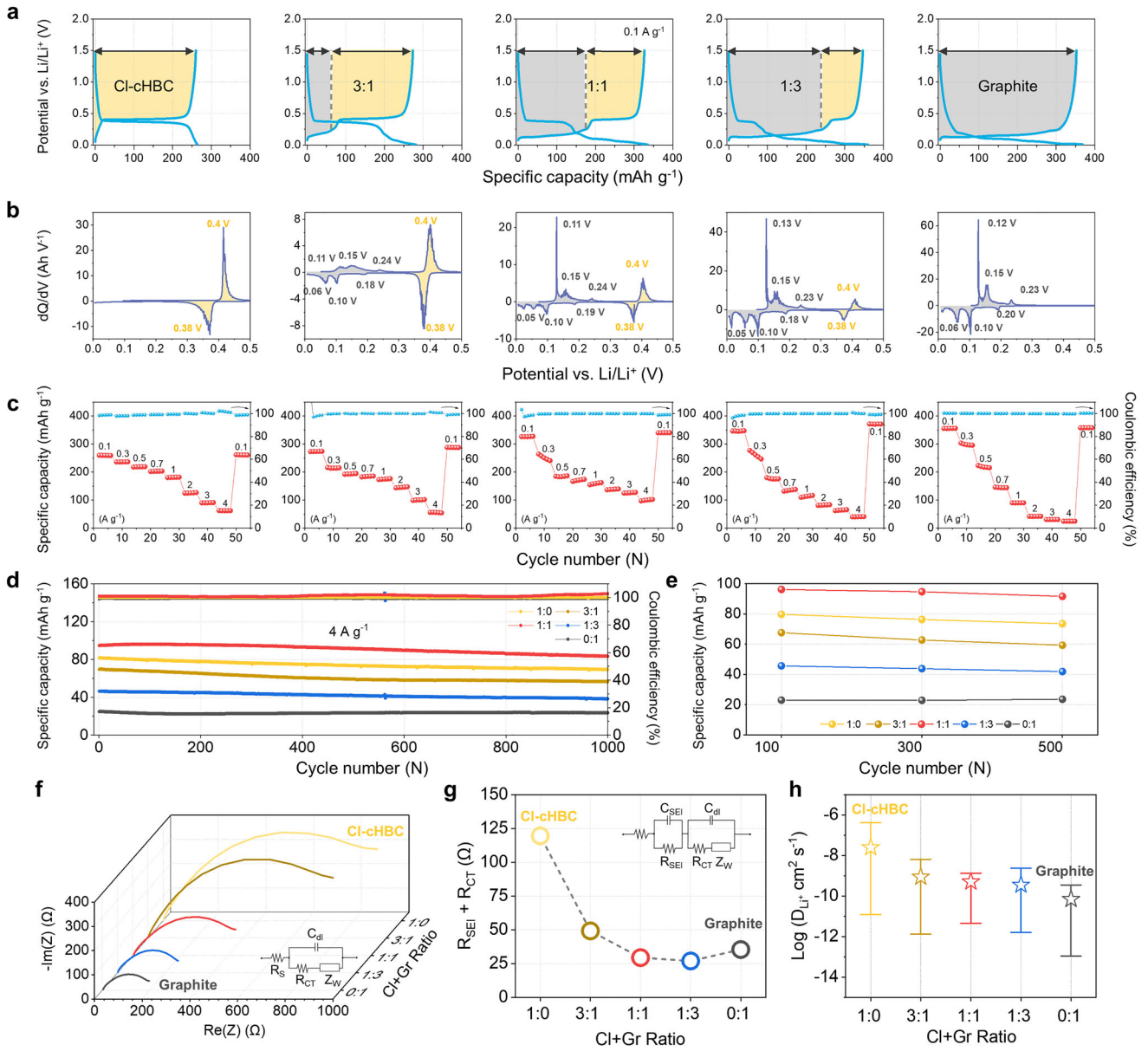

Figure 3. a) Galvanostatic charge/discharge plots and b) corresponding differential capacity curves of Li metal half-cells with pristine Cl-cHBC, 3:1, 1:1, 1:3, and pristine MCMB graphite anodes. The yellow and grey shaded regions in a) indicate the contribution of Cl-cHBC and graphite, respectively, in the hybrid anodes. c) Rate capability and d) cycling performance of pristine Cl-cHBC, 3:1, 1:1, 1:3, and pristine MCMB graphite anodes. e) Specific capacity plots of pristine Cl-cHBC, 3:1, 1:1, 1:3, and pristine MCMB graphite anodes after 100, 300, and 500 cycles at 4.0 A g^{-1}. f) Nyquist plots before cycling and g) the combined R_{SEI} and R_{CT} values after cycling for pristine Cl-cHBC, 3:1, 1:1, 1:3, and pristine MCMB graphite anodes in Li metal half-cell structure, measured over a frequency range from 1×10^6 to 1×10^{-1} Hz. h) Diffusion coefficient (D_{Li}) plots for pristine Cl-cHBC, 3:1, 1:1, 1:3, and pristine MCMB graphite anodes.

yellow shaded region) gradually decreases as the MCMB graphite content (gray shaded region) increases from a ratio of 3:1 to 1:3. Further insight into the individual contributions of Cl-cHBC and MCMB was gained by analyzing the differential capacity (dQ/dV) (Figure 3b). The dQ/dV curves corroborate the galvanostatic results and show that the peak at 0.38 V, corresponding to Cl-cHBC redox activity, progressively decreases with increasing MCMB ratio. Conversely, distinct peaks at 0.19, 0.10, and 0.05 V, which are associated with the well-known staging behavior of MCMB graphite, become more pronounced with higher MCMB content.

2.6. Rate Performance and Long-Term Stability of Hybrid Anodes in A Half-Cell

To demonstrate the advantages of our hybrid anodes, the rate capability of three blend ratio samples was examined under various

current densities ranging from 0.1 to 4 A g^{-1} (Figure 3c; Figure S12, Supporting Information). Among the tested samples, the 1:1 hybrid anode showed the most remarkable performance. In particular, at a high current density of 4 A g^{-1}, the 1:1 hybrid anode achieved specific capacities of ≈100 mAh g^{-1}, 1.8, and 2.5 times higher than those of the 3:1 and 1:3 hybrid anodes, respectively. In particular, the 1:1 hybrid anode exhibited a 4.2-fold higher capacity compared with the pristine MCMB anode at the same high current density (Table S2 and Figure S13, Supporting Information). Interestingly, with increasing current density, the discharge profiles showed that the contribution of Cl-cHBC became increasingly dominant, especially at higher current densities (Figure S14, Supporting Information). This behavior highlights the superior rate capability of Cl-cHBC, which effectively complements the capacity contribution of MCMB graphite, resulting in improved overall performance under demanding conditions. In addition to rate capability, the long-term cycling stability of the 1:1 hybrid anode was also evaluated to assess its durability (Figure 3d). The hybrid anode maintained a reversible specific capacity of ≈95 mAh g^{-1} at a constant current of 4 A g^{-1} and sustained a specific capacity of 85 mAh g^{-1} even after 1000 cycles, corresponding to a capacity retention of 90%. In sharp contrast, the pristine MCMB anode exhibited a much lower specific capacity of ≈25 mAh g^{-1} under the same conditions. Post-mortem TEM and XRD analyses also confirmed the structural retention of the 1:1 Cl-cHBC/graphite hybrid anode even after 1000 cycles at 4 A g^{-1} (Figure S15a–c, Supporting Information). The lattice fringes and diffraction patterns showed no significant change, indicating the excellent structural robustness and long-term stability of the hybrid anode (Figures S9 and S15d, Supporting Information). XPS measurements of the Li 1s, F 1s, and C 1s regions were also performed on the pristine Cl-cHBC, Cl-cHBC/graphite (1:1), and graphite anodes after 1000 cycles (Figure S16, Supporting Information). The spectra showed the presence of stable inorganic SEI components, such as Li_2CO_3 and LiF, in all samples, indicating that the formation of such SEI layers likely contributes to the observed cycling stability. Further insights into the cycling behavior were obtained from the differential capacity (dQ/dV) analysis, which showed that the 1:1 hybrid anode retained almost identical peak shapes even after 300 cycles (Figure S17, Supporting Information).[56] Thus, it is reasonable to conclude that the 1:1 hybrid anode has superior specific capacity, outstanding rate capability, and excellent cycling stability compared to the other blend ratios. In addition, rate capability tests using a standard electrolyte without FEC additive (1.0 M $LiPF_6$ in EC/DEC = 50/50 v/v) also showed comparable performance, demonstrating that stable operation is possible even without FEC (Figure S18, Supporting Information). Furthermore, a 1:1 hybrid anode was fabricated without incorporating an additional conducting agent, as the intrinsically high conductivity of the MCMB graphite in the hybrid anode provided sufficient electrical conductivity (Figure S19, Supporting Information). Remarkably, the electrochemical performance of the 1:1 hybrid anode without a conducting agent was still better than that of the other samples, indicating that the inclusion of additional conducting agents is unnecessary. In particular, the 1:1 hybrid anode achieved a high areal capacity of 2.15 mAh cm^{-2} while maintaining excellent electrochemical performance. This demonstrates that it is suitable for practical, high-energy-density applications and, in particular, overcomes the limitations associated with the inherently low tap density of curved nanographene (Figure S20, Supporting Information).

2.7. Electrochemical Analyses of Hybrid Anodes

To gain deeper insights into our hybrid anodes, electrochemical impedance spectroscopy (EIS) measurements were performed to analyze the charge transfer resistance (R_{CT}) using Nyquist plots for both the pristine and hybrid anodes (Figure 3f). The resulting plots revealed a substantial increase in the charge transfer resistance (R_{CT}), from ≈200–900 Ω, as the Cl-cHBC ratio increased from 0:1 to 1:0. This increase can be attributed to the inherently lower conductivity of Cl-cHBC compared to graphite. In contrast, the hybrid anodes, especially those with 1:1 and 1:3 ratios, exhibited significantly lower R_{CT} values, indicating the positive effect of the conductive graphite phase in facilitating charge transfer. Moreover, all the hybrid anodes showed a marked reduction in impedance values after prolonged cycling. In particular, the 1:1 and 1:3 hybrid anodes exhibited the lowest impedance values of ≈25 Ω (Figure 3g), suggesting that the stable composite structure and good electrical connectivity are maintained throughout cycling, further contributing to improved electrochemical performance. To complement the EIS analysis, the Li-ion diffusion coefficient (D_{Li}) of the hybrid anodes was monitored using the galvanostatic intermittent titration technique (GITT) during discharge and charge cycles at a constant current density of 0.1 C, within a voltage range of 0.005–1.5 V (Figure 3h; Figure S21, Supporting Information). Among all samples, the pristine Cl-cHBC anode (1:0 ratio) exhibited the highest average D_{Li}, ≈2.5×10^{-8} cm^2 s^{-1}, which can be attributed to the large *d*-spacing and short diffusion pathways. The 3:1, 1:1, and 1:3 hybrid anodes also exhibited significantly higher D_{Li} values, in the range of 10^{-10} cm^2 s^{-1}, than the pristine MCMB graphite anode (Table S3, Supporting Information). Importantly, the 1:1 hybrid anode exhibited the most stable D_{Li} behavior, with minimal fluctuations between the maximum and minimum values during lithiation and the delithiation cycles (Figure 3h; Figure S22, Supporting Information).[57] The trends observed in both the EIS and GITT measurements demonstrate the advantages of the composite design, which simultaneously reduces charge transfer resistance and improves Li-ion diffusion compared to the individual pristine Cl-cHBC or MCMB graphite anodes. In addition, the electronic conductivity, as determined by four-point probe measurements of sheet resistance (Figure S23, Supporting Information), showed a clear decrease in resistance with increasing graphite content. This improvement, which complements the improved ionic transport, contributes to the well-balanced electrochemical performance of the hybrid anode.

Further electrochemical analysis was performed using cyclic voltammetry (CV) to probe the redox behavior and reaction kinetics of the pristine and hybrid anodes. CV measurements were performed at scan rates ranging from 0.1 to 0.45 mV s^{-1} within a potential window of 0.005–1.5 V (Figure S24a–e, Supporting Information). The CV curves of the 1:1 hybrid anode clearly show four distinct anodic and cathodic peaks, corresponding to the redox processes of Cl-cHBC (0.444 V and 0.323 V) and MCMB graphite (0.218 and 0.005 V), respectively (Figure S24c, Supporting Information). In addition, the *b*-values were analyzed from

the slope of the log(i_p) versus log(v) plots, where i_p is the peak current and v is the scan rate. Based on the relation $i_p = av^b$, b-values of 0.44/0.58 for the anodic peaks and 0.52/0.61 for the cathodic peaks were obtained for the 1:1 hybrid anode (Figure S24h, Supporting Information).[58] These values indicate that the Li storage process in the hybrid anode predominantly followed a diffusion-controlled mechanism (Figure S24f–j, Supporting Information). In addition, linear sweep voltammetry (LSV) measurements were performed at a scan rate of 1.0 mV s^{-1} to evaluate the electrochemical stability of the hybrid anode (Figure S25, Supporting Information). The obtained LSV plots show high electrochemical stability, indicating potential compatibility with high-voltage cathodes without significant degradation. Thus, the EIS, GITT, CV, and LSV analyses confirmed that the 1:1 hybrid anode offers a well-balanced combination of low resistance, fast Li-ion diffusion, electrochemical stability at high voltage, and stable diffusion-controlled Li storage behavior.

2.8. Li Insertion Mechanism of Hybrid Anode Revealed by Theoretical Calculations

To gain fundamental insights into the Li insertion mechanism of the hybrid anode, we investigated the Li affinity of the constituents (i.e., Cl-cHBC and graphite) in the hybrid anode using Monte Carlo (MC) simulations and density functional theory (DFT) calculations (see Computational details in the ESI†). The crystalline structure of Cl-cHBC was modeled based on previously reported data, whereas the graphite structure was constructed by stacking multiple graphene layers.[34] MC simulations were first used to identify the stable and energetically favorable Li adsorption sites within both materials. The results showed that crystalline Cl-cHBC contained two accessible and stable Li adsorption sites, labeled A1 and A2 (Figure S26a, Supporting Information), whereas graphite had a single Li adsorption site, labeled B1 (Figure S26b, Supporting Information). Once the adsorption sites were identified, calculations showed that Cl-cHBC had a stronger average Li binding energy—≈0.4 eV higher—than graphite (Figure S27, Supporting Information). This stronger Li interaction indicates that Cl-cHBC has a higher affinity for Li-ions than graphite. These results suggest that Li-ions are more likely to be preferentially inserted into the Cl-cHBC regions during the charging process before occupying the graphite layers.

Next, the composite structure was modeled based on the crystalline Cl-cHBC and graphite structures while minimizing the lattice mismatch (i.e., f) between the two structures (i.e., $f_x = -0.042\%, f_y = 0.041\%, f_a = 0.002\%$, where x and y are the box length and a is the area) to observe the Li affinity in the composite structure (Figure S28a, Supporting Information). With this optimized composite structure, MC simulations were performed to identify the accessible and energetically favorable Li adsorption sites. The simulations revealed four distinct types of stable adsorption sites within the composite (Figure S28b, Supporting Information): i) sites a1–a4 are located between stacked Cl-cHBC layers, ii) site b1 is situated between the Cl-cHBC and graphite layers, iii) sites c1–c2 are positioned between adjacent Cl-cHBC columns, and iv) site d1 is located within the graphite layers (Figure S28b, Supporting Information). Subsequent DFT calculations of the Li binding energies at these sites indicated that the strongest Li interaction occurred in the interlayer spaces between the stacked Cl-cHBC molecules, followed by the next most favorable adsorption sites in the interfacial regions between Cl-cHBC and graphite (Figure S29, Supporting Information). These results indicate that during initial Li insertion, the Li ions preferentially occupied the interlayer spaces of Cl-cHBC and the interfaces between Cl-cHBC and graphite.

Building on the identification of preferential Li adsorption sites within the hybrid anode, the Li insertion mechanism was calculated, and the corresponding structural and voltage changes during the charging process were theoretically monitored. To determine the sequence of Li insertion, the formation energy at each step was calculated as a function of Li content (**Figure 4a,c**). The calculated formation energies revealed that the energy differences between the insertion sites gradually decreased as the number of inserted Li atoms increased. Finally, the formation energy stabilized at ≈−62.40 kcal mol^{-1} when the Li content reached 96 atoms, indicating a thermodynamically stable state. In addition, the theoretical voltage profile was plotted as a function of Li insertion and directly compared with the experimental galvanostatic charge curves for the 1:1 hybrid anode (Figure 4b). The comparison revealed excellent agreement in identifying the different Li insertion stages. In the initial stage (Stage I in Figure 4c), Li is preferentially inserted into the interlayer spaces of stacked Cl-cHBC molecules and at the interfaces between the Cl-cHBC and graphite layers. As the Li insertion progressed to Stage II, the remaining Li atoms occupied the spaces between the Cl-cHBC columns and began to penetrate into the graphite layers. Remarkably, in this stage, both the theoretical voltage profile and the experimental charge curve exhibit a plateau region, corresponding to a steady potential output of ≈0.47 V, which can be attributed to Li insertion between Cl-cHBC columns. In the final stage (Stage III), Li insertion occurred predominantly within the graphite layers. Accordingly, the voltage profile shows a gradual decrease, reflecting the typical behavior of Li intercalation into graphite. There is a slight discrepancy between the experimental and calculated voltage profiles. This discrepancy is due to the fact that the theoretical model does not take into account kinetic factors such as the Li-ion transport resistance within the electrolyte, which leads to a voltage drop in the experimental measurements, especially at the beginning of the charging process.[60] To this end, the sequential Li insertion mechanism in the Cl-cHBC/graphite hybrid anode begins with Li preferentially occupying the stacked Cl-cHBC layers, followed by the interfacial sites between Cl-cHBC and graphite, between the Cl-cHBC columns, and finally the graphite layers. Furthermore, to provide a more comprehensive mechanistic understanding, we performed additional theoretical analyses beyond the Li insertion energetics. DFT calculations of Li migration barriers revealed that interfacial regions in the Cl-cHBC/graphite composite lower the migration energy compared to single-component anodes, indicating the synergistic role of the hybrid interface in facilitating Li-ion transport (Figure S30, Table S5, Supporting Information). All-atom molecular dynamics simulations further confirmed that the composite exhibits intermediate Li diffusivity (between Cl-cHBC and graphite), moderated volume expansion, and balanced shear modulus during

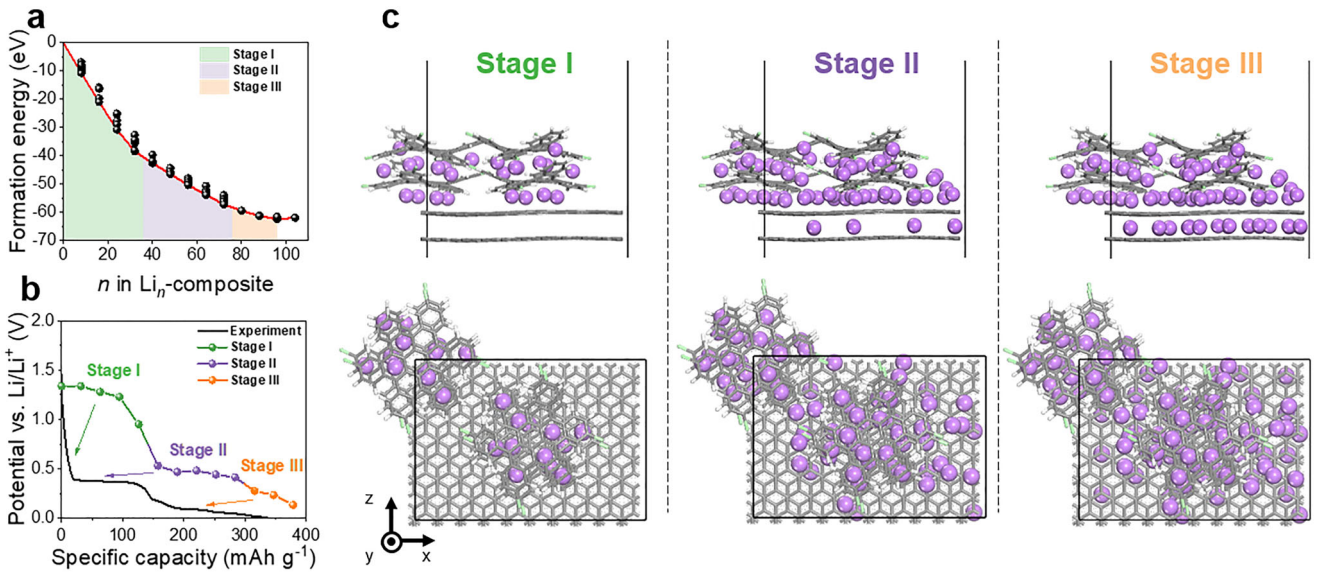

Figure 4. a) Formation energies of Li intercalated Cl-cHBC/graphite composite at different Li contents. The red lines indicate the convex hull of the lowest formation energy at each Li content. b) Calculated voltage profiles with galvanostatic charge plots containing a 1:1 hybrid anode. Each arrow in the voltage profile represents the corresponding stage of the experimental result. c) Projection and top views from stage I to III represent the atomic configuration of the Li intercalated Cl-cHBC/graphite composite. Each configuration corresponds to the region from stage I to III at the formation energy plot and voltage profile. The atoms of Cl-cHBC and graphite are presented with a stick model, while the Li atoms are represented with spheres. The Li, C, Cl, and H atoms are colored purple, gray, green, and white, respectively.

lithiation (Figures S31–S33, Supporting Information). These results demonstrate that the hybrid anode balances Li-ion mobility and structural stability through the complementary functions of Cl-cHBC and graphite. To experimentally validate the calculated Li insertion sequence, in situ XRD and Raman measurements were performed during the lithiation/delithiation of the 1:1 hybrid anode (Figure S34, Supporting Information). The in situ XRD patterns showed that the (002) diffraction peak of MCMB graphite at $2\theta = 26.5°$ remained unchanged during the initial Li insertion into Cl-cHBC, shifted slightly to 26.4° at the beginning of Li intercalation into graphite, and then gradually migrated further, consistent with LiC_{12} formation. Complementary in-situ Raman spectra using 325 nm excitation laser revealed a reversible blue shift of the G-band as Li intercalated into the graphite layers, while the D band remained unchanged. These results support the sequential Li insertion pathway, confirming that Li first occupies Cl-cHBC and interfacial sites before progressing into the graphite domains.

2.9. Electrochemical Performance of Hybrid Anodes in A Full-Cell

To investigate the applications of our hybrid anode in LIBs, its electrochemical performance was evaluated in a full-cell configuration using a single-crystal NCM811 cathode. For a direct comparison, full cells with pristine MCMB graphite and Cl-cHBC anodes were monitored under identical conditions. Both reference cells exhibited typical discharge and charge voltage trajectories within the range of 2.8–4.3 V and delivered comparable specific capacities of ≈190 mAh g^{-1} (Figure S35, Supporting Information). **Figure** 5a shows the galvanostatic discharge and charge profiles of the 1:1 hybrid anode paired with the NCM811 cathode. The composite-based full-cell achieved a specific capacity of ≈200 mAh g^{-1}. The voltage profile also gives a clear insight into the contribution of the individual components in the composite, which corresponds to the capacity of MCMB graphite, where the yellow-shaded region represents the contribution from Cl-cHBC. It is noteworthy that a distinct hump appears at ≈90 mAh g^{-1}, representing the transition from graphite to Cl-cHBC upon lithiation (or delithiation). Importantly, despite the inclusion of Cl-cHBC, the overall voltage profile of the hybrid anode-based full cell was very similar to that of the pristine Graphite/NCM811 system, suggesting that there was no significant voltage penalty. This indicates that the Cl-cHBC component was highly compatible with the NCM811 cathode and did not adversely affect the voltage window or stability. The rate capability of the full-cells was further characterized by varying the C-rate range from 0.1 to 7 C (Figure 5b,c). Reversible specific capacities of 190, 150, 135, 100, and 75 mAh g^{-1} were observed at C-rates 0.1, 1.0, 2.0, 5.0, and 7.0, respectively, and fully recovered when the current rate returned to 0.1 C. Compared to full cells with pristine MCMB graphite and Cl-cHBC anodes, the 1:1 hybrid anode consistently exhibited superior specific capacities, especially at high C-rate conditions. This demonstrates that the optimum blend ratio provides an excellent balance between capacity, rate capability, and voltage stability in full-cell applications (Figure S36, Supporting Information).

The cyclic endurance of our hybrid anodes was further investigated under a high-rate condition of 5 C to evaluate their long-term durability (Figure S37, Supporting Information). Surprisingly, the hybrid anode maintained a specific capacity of 60 mAh g^{-1} after 1000 cycles, which significantly outperformed the pristine MCMB graphite anode that maintained only ≈20 mAh g^{-1}, while consistently exhibiting a stable

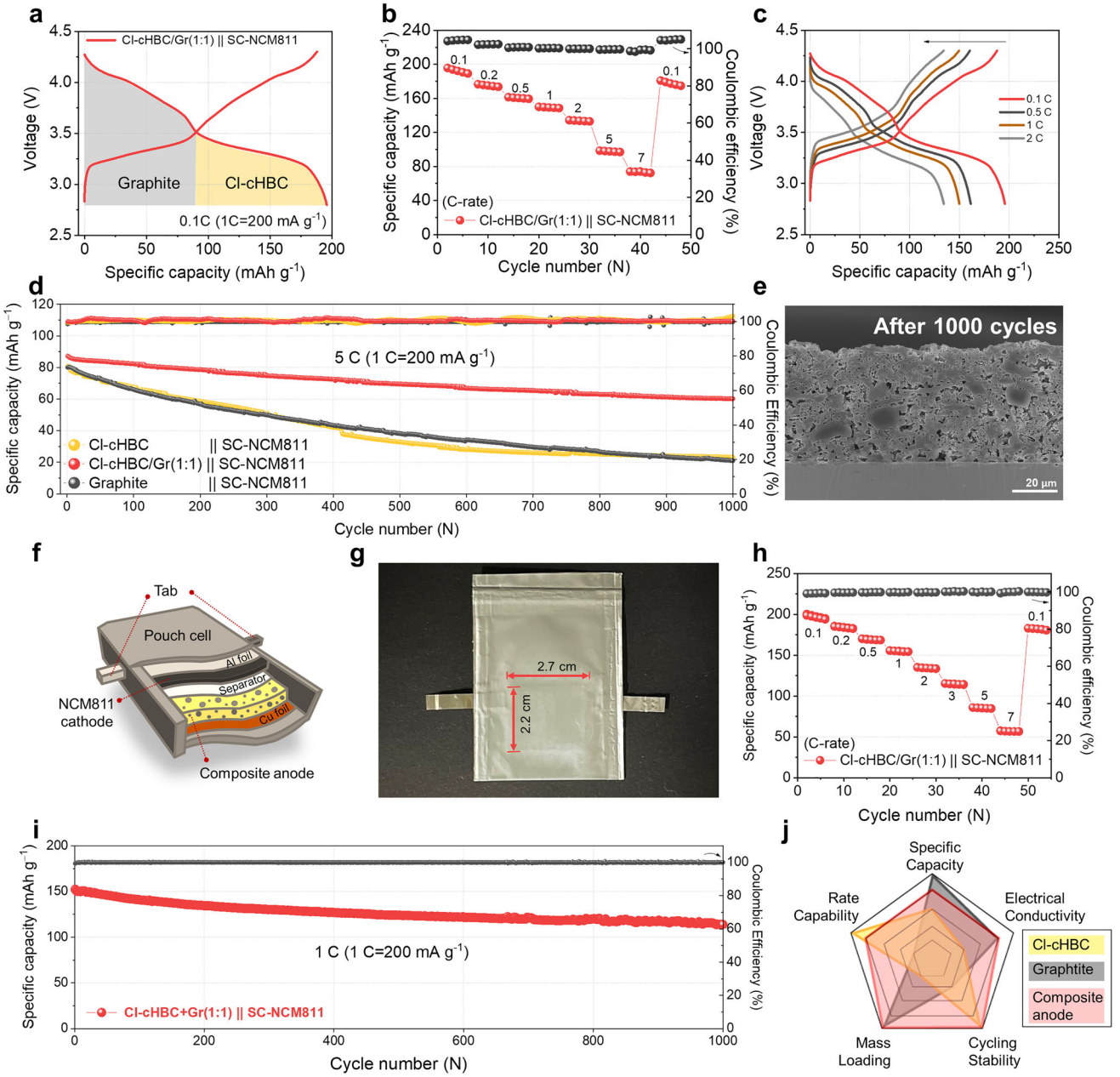

Figure 5. a) Galvanostatic charge/discharge curves of full-cells with an SC-NCM811 cathode paired with a 1:1 hybrid anode. The yellow and gray shaded regions represent the contribution of Cl-cHBC and graphite, respectively. b) Rate capability of full-cells incorporating the 1:1 hybrid anode. c) Galvanostatic discharge and charge profiles of the full-cells with the 1:1 hybrid anode at various C-rates. d) Long-term cycling performance of full-cells with pristine Cl-cHBC, 1:1 composite, and pristine MCMB graphite anodes at a high current rate of 5 C. e) Cross-sectional SEM image of the 1:1 hybrid anode after 1000 cycles at 5 C. f) Schematic representation of the pouch cell configuration with SC-NCM811 cathode and 1:1 hybrid anode. g) Digital photograph of the assembled pouch cell with SC-NCM811 cathode and 1:1 hybrid anode. h) Rate capability performance of the pouch cell evaluated at various C-rates. i) Long-term cycling stability of the pouch cell. j) Radar charts comparing the performance parameters of Cl-cHBC, graphite, and hybrid anodes.

Coulombic efficiency of 99% throughout the cycling period (Figure 5d). These results clearly demonstrate the excellent cyclic endurance and structural robustness of the hybrid anode, especially under demanding cycling conditions. The improved cycling performance of the hybrid anode compared to the graphite or Cl-cHBC anodes can be attributed to the synergistic interaction between the two components. The combination of the high electrical conductivity of MCMB graphite and the large interlayer spacing of Cl-cHBC enabled uniform Li-ion diffusion throughout the electrode. This uniform ion transport effectively reduces the Li-ion diffusion resistance and suppresses localized overpotentials during repeated charge-discharge cycles. As a result, mechanical stress and structural degradation were effectively mitigated, leading to improved cycling stability and minimal

capacity fading over extended operation.[61] To further substantiate these findings, post-mortem morphological analysis was performed after 1000 cycles at 5 C using cross-sectional SEM imaging. As shown in Figure 5e, the hybrid anode retains its structural integrity with minimal morphological changes and no significant particle pulverization or surface roughening. In contrast, the pristine MCMB graphite anode exhibits pronounced structural degradation, characterized by the breakdown of its spherical morphology and increased surface roughness (Figure S38, Supporting Information). These observations confirm that the optimized composite architecture not only improves electrochemical performance but also maintains mechanical stability during prolonged cycling, thus providing a reliable strategy for achieving durable and high-rate LIB anodes. Furthermore, our hybrid anode demonstrated superior full-cell electrochemical performance when benchmarked against recently developed anodes reported in the literature, further confirming the effectiveness of this composite approach (Figure S39, Supporting Information).

To further validate the practical applicability of our 1:1 hybrid anode, a pouch cell with an electrode area of 2.2 × 2.7 cm^2 was fabricated (Figure 5f,g). The pouch cell, paired with the NCM811 cathode, was tested at different C-rates ranging from 0.1 to 7 C (Figure 5h). At a low C-rate of 0.1 C, the pouch cell delivered a specific capacity of 200 mAh g^{-1}, closely matching the performance observed in the coin cell tests. This agreement demonstrates the excellent scalability of the hybrid anode without a drop in performance when transitioning to a larger-format cell. In addition, the pouch cell showed stable rate performance even under high C-rate conditions. Reversible specific capacities of ≈135 mAh g^{-1} at 2 C and 90 mAh g^{-1} at 5 C were maintained, indicating that the electrochemical performance is well preserved even under high-rate conditions. In addition to rate performance, the long-term cycling stability of the pouch cell was also thoroughly investigated. Remarkably, the hybrid anode sustained a stable discharge capacity of ≈115 mAh g^{-1} over 2100 cycles at 1 C, corresponding to over 2600 h of continuous operation, while maintaining a high Coulombic efficiency of 99%. Radar charts were constructed to provide a comprehensive comparison of the electrochemical performance of the hybrid anode with its individual components (Figure 5j). The hybrid anode consistently outperformed both the pristine MCMB graphite and Cl-cHBC anodes across multiple performance metrics, including specific capacity, rate capability, and cycling stability, effectively accounting for the inherent limitations of each constituent material. These results highlight the potential of the optimized hybrid anode for high-performance LIB applications, especially for fast-charging and long-duration scenarios.

3. Conclusion

In conclusion, we successfully demonstrated the synergistic effect of a hybrid anode integrating highly crystalline curved-nanographene and graphite in high-performance LIBs. The optimized 1:1 blend of Cl-cHBC and MCMB resulted in a smooth, dense, and homogeneous morphology that effectively exploited the complementary strengths of the two materials. This structural integration resulted in significantly improved rate capability and long-term cycling stability. To gain fundamental insights, the Li insertion mechanism within the Cl-cHBC/graphite hybrid anode was systematically analyzed using DFT calculations and MC simulations. The theoretical analysis confirmed that Li insertion proceeds sequentially through the anode, highlighting the well-coordinated Li-ion pathways within the hybrid structure. In addition, the electrochemical characteristics of the half-cell configuration further validated the superior performance of the hybrid anodes. The optimized composite delivered a specific capacity of 100 mAh g^{-1} at a high current density of 4 A g^{-1}, markedly outperforming the pristine MCMB graphite anode (≈20 mAh g^{-1} at 4 A g^{-1}). The excellent performance of the hybrid anode was further substantiated by full-cell tests, paired with a single-crystal NCM811 cathode. The hybrid anode-based full-cell demonstrated outstanding rate capability, delivering 100 mAh g^{-1} at 5 C, along with excellent cycling stability, retaining 70% of its initial capacity after 1000 cycles at 5 C. In particular, the successful integration of the hybrid anode into the pouch cell formats has reinforced its scalability and practical viability. The pouch cell remained stable over 2100 cycles at 1 C and achieved a discharge capacity of ≈115 mAh g^{-1} with a high Coulombic efficiency of 99%. These comprehensive results highlight the effectiveness of our hybrid anode in overcoming the limitations of both pristine Cl-cHBC and MCMB graphite anodes and offer a promising solution for next-generation LIBs, while further optimization could unlock their potential for operation under sub-ambient conditions.

4. Experimental Section

Materials: Cl-cHBC was synthesized using a previously reported method. Mesocarbon microbeads (MCMB) were purchased from MTI. Poly(vinylidene fluoride) (PVDF, Mw = 1 000 000 g mol^{-1}) and Super C45 powder were sourced from Solef and TIMCAL, respectively. N-methyl-2-pyrrolidone (NMP) was procured from Sigma-Aldrich Co., Ltd. Single-crystal $LiNi_{0.8}Co_{0.1}Mn_{0.1}O_2$ (SC-NCM811) was supplied by SM-LAB. Polypropylene membranes (Celgard 2400) were used as separators, and 2032-type coin cells were acquired from Wellcos Co. Electrolytes consisting of 1.3 M $LiPF_6$ in ethylene carbonate/diethyl carbonate (EC/DEC, 3:7 v/v) with 10 wt.% fluoroethylene carbonate (FEC) were obtained from Soulbrain Co., Ltd.

Characterization Methods: The synthesized Cl-cHBC was characterized by ^{1}H-NMR (Agilent NMR 600 MHz Liquid System, Agilent). The surface and cross-sectional morphology of the Cl-cHBC and MCMB graphite hybrid anodes were analyzed by scanning electron microscopy (SEM; SU8220 Cold FE-SEM, Hitachi). For elemental distribution analysis, energy-dispersive X-ray spectroscopy (EDS) mapping was performed using an OCTANE PLUS EDS detector (AMETEK EDAX) attached to the SEM system. SEM cross-sectional samples were prepared using an ion milling system (IM4000, Hitachi) to obtain clear images of the internal structure. Grazing-incidence wide-angle X-ray scattering (GIWAXS) measurements were conducted at the 6D UNIST-PAL beamline of the Pohang Accelerator Laboratory (Pohang University of Science and Technology, Republic of Korea) to analyze the crystalline structures of the hybrid anodes and investigate the influence of different Cl-cHBCs on the MCMB graphite ratios. For the GIWAXS analysis, electrode slurries were coated onto silicon wafers, and the samples were irradiated with monochromatic X-rays (wavelength λ = 1.0722 Å) at a fixed grazing incidence angle of 0.12^0 for 1 min. 3D X-ray microscopy (3D-XRM; Xradia 520 Versa/810 Ultra, Zeiss) was used to visualize the internal structure and distribution of Cl-cHBC and MCMB graphite in the hybrid anodes in 3D. High-resolution transmission electron microscopy (HR-TEM, Titan G2 Cube 60–300, FEI) was used to further investigate the detailed morphology of the hybrid

anodes and to analyze the interlayer spacing (d-spacing) of the constituent materials.

Electrode Preparations: As a working electrode, the Cl-cHBC/graphite hybrid anode was composed of 80 wt.% active material, consisting of a combination of Cl-cHBC and graphite. The hybrid anode was prepared by mixing Cl-cHBC and graphite in ratios of 1:0 to 0:1 (1:0–Cl-cHBC 80 wt.%, graphite 0 wt.%; 3:1–Cl-cHBC 60 wt.%, graphite 20 wt.%; 1:1–Cl-cHBC 40 wt.%, graphite 40 wt.%; 1:3–Cl-cHBC 20 wt.%, graphite 60 wt.%; 0:1–Cl-cHBC 0 wt.%, graphite 80 wt.%). In addition, 10 wt.% Super C45 was used as a conductive agent and 10 wt.% PVDF in NMP as a binder. These components were mixed in a ball mill for 30 min, and the uniformly mixed slurry was cast onto Cu foil using the doctor blade method. Then, the casted electrode was dried in a vacuum oven at 120 °C for 12 h to remove any residual solvent. To improve crystallinity, the hybrid anode was thermally annealed in an Ar-filled tube furnace at 330 °C for 50 min. The average mass loading of the electrodes was 2.3–3.0 mg cm^{-2}. Under high mass-loading conditions, the electrode was fabricated with a loading of ≈9.0 mg cm^{-2}. The SC-NCM811 cathode was prepared using the same procedure as described above, with the only difference being that it was cast onto aluminum foil.

Electrochemical Performance Measurements: The electrochemical performances of the hybrid anodes were evaluated in both half-cell and full-cell configurations. For the half-cell measurements, 2032-type coin cells were assembled in an argon-filled glove box. The working electrode was prepared with a hybrid anode, and a Li foil was used as the counter electrode. Polypropylene membranes (Celgard 2400) served as separators and an electrolyte consisting of 1.3 M $LiPF_6$ in EC/DEC (3:7, v/v) with 10 wt.% FEC was used.

Galvanostatic charge–discharge measurements were performed using a battery tester (WBCS3000S, Wonatech) over a voltage range of 0.005–1.5 V versus Li/Li^+ at various current densities.

A single-crystal NCM811 electrode was used as the cathode for the full-cell tests. Before assembly, the hybrid anodes were pre-cycled to form a stable solid electrolyte interphase (SEI) layer. The negative-to-positive (N/P) capacity ratio of the full cells was carefully controlled between 1.0 and 1.2 to ensure balanced capacity utilization. The electrochemical performance of the full cell was evaluated over a range of current densities within a voltage window of 2.8–4.3 V.

Electrochemical impedance spectroscopy (EIS), cyclic voltammetry (CV), and linear sweep voltammetry (LSV) were performed with a multichannel potentiostat (BioLogic VSP-300). EIS measurements were recorded in the frequency range of 1×10^6 to 1×10^{-1} Hz, with an AC amplitude voltage of 14.2 mV, applied to evaluate charge transfer resistance and impedance evolution. CV measurements were performed in a voltage range of 0.005–1.5 V at different scan rates to analyze the redox behavior and kinetic properties. LSV measurements were performed at a scan rate of 1.0 mV s^{-1}.

The Li-ion diffusion coefficient (D_{Li}) was determined using the galvanostatic intermittent titration technique (GITT). The D_{Li} was calculated using the following equation:

$$D_{Li} = \frac{4L^2}{\pi\tau}\left(\frac{\Delta E_s}{\Delta E_\tau}\right)^2, \left(\tau \lll \frac{L^2}{D_{Li}^2}\right) \quad (1)$$

τ is the duration of the current pulse, and L represents the electrode thickness. ΔE_s represents the change in the steady-state voltage and ΔE_τ is the total change in the cell voltage during the constant current pulse.

Supporting Information

Supporting Information is available from the Wiley Online Library or from the author.

Acknowledgements

This study was supported by the National Research Foundation (NRF) of Korea, funded by the Ministry of Science and Information & Communication Technology (RS-2025-16064954), the Korea Institute of Science and Technology Open Research Program (2E33503), and a grant from the Commercialization Promotion Agency for R&D Outcomes (COMPA) funded by the Ministry of Science and ICT, 2023, RS-2023-00304729). S.K.K. acknowledges the financial support from RS-2023-00257666 and computational resources from UNIST-HPC and KISTI (KSC-2024-CRE-0327). This work was supported by the 2025 Research Fund (1.250009.01) of Ulsan National Institute of Science & Technology (UNIST). We thank UCRF (UNIST Central Research Facilities) for support in using the equipment.

Conflict of Interest

The authors declare no conflict of interest.

Author Contributions

H.C., M.K., and S.H.O. contributed equally to this work. H.C. and S.J.K. conceived the study and designed the experiments. H.C. characterized the samples and performed all electrochemical experiments. M.K. synthesized the materials, characterized the samples with S.A., supervised the process, and provided insights. J.H.H. and J.J. analyzed the experimental results. S.H.O. and D. H.K. conducted MC simulations and DFT calculations, and S.K.K. supervised and provided insights. S.J.K. supervised the study. The manuscript was written by all the authors. All the authors approved the final version of the manuscript.

Data Availability Statement

The data that support the findings of this study are available from the corresponding author upon reasonable request.

Keywords

contorted hexabenzocoronene, curved nanographene, hybrid anode, Li-ion battery, organic anode

Received: June 11, 2025
Revised: August 21, 2025
Published online:

[1] M. Armand, J. M. Tarascon, *Nature* **2008**, *451*, 652.
[2] V. Etacheri, R. Marom, R. Elazari, G. Salitra, D. Aurbach, *Energy Environ. Sci.* **2011**, *4*, 3243.
[3] G. Jeong, Y.-U. Kim, H. Kim, Y.-J. Kim, H.-J. Sohn, *Energy Environ. Sci.* **2011**, *4*, 1986.
[4] M. Li, J. Lu, Z. Chen, K. Amine, *Adv. Mater.* **2018**, *30*, 1800561.
[5] J. Lu, Z. Chen, Z. Ma, F. Pan, L. A. Curtiss, K. Amine, *Nat. Nanotechnol.* **2016**, *11*, 1031.
[6] Y. Li, Y. Lu, P. Adelhelm, M.-M. Titirici, Y.-S. Hu, *Chem. Soc. Rev.* **2019**, *48*, 4655.
[7] M. Winter, J. O. Besenhard, M. E. Spahr, P. Novák, *Adv. Mater.* **1998**, *10*, 725.
[8] L. Zhao, B. Ding, X.-Y. Qin, Z. Wang, W. Lv, Y.-B. He, Q.-H. Yang, F. Kang, *Adv. Mater.* **2022**, *34*, 2106704.
[9] Y. Liu, Y. Zhu, Y. Cui, *Nat. Energy* **2019**, *4*, 540.
[10] Y. Liu, H. Shi, Z.-S. Wu, *Energy Environ. Sci.* **2023**, *16*, 4834.
[11] Y. Yin, Y. Peng, J. Chen, Y. Wang, X. Dong, Y. Xia, *Adv. Funct. Mater.* **2024**, *34*, 2403682.

[12] M. Ko, S. Chae, J. Ma, N. Kim, H.-W. Lee, Y. Cui, J. Cho, *Nat. Energy* **2016**, *1*, 16113.
[13] N. Kim, S. Chae, J. Ma, M. Ko, J. Cho, *Nat. Commun.* **2017**, *8*, 812.
[14] S. Chae, S.-H. Choi, N. Kim, J. Sung, J. Cho, *Angew. Chem., Int. Ed.* **2020**, *59*, 110.
[15] J. Müller, M. Abdollahifar, A. Vinograd, M. Nöske, C. Nowak, S.-J. Chang, T. Placke, W. Haselrieder, M. Winter, A. Kwade, *Chem. Eng. J.* **2021**, *407*, 126603.
[16] P. Li, H. Kim, S.-T. Myung, Y.-K. Sun, *Energy Storage Mater.* **2021**, *35*, 550.
[17] M. N. Obrovac, V. L. Chevrier, *Chem. Rev.* **2014**, *114*, 11444.
[18] M. T. McDowell, S. W. Lee, W. D. Nix, Y. Cui, *Adv. Mater.* **2013**, *25*, 4966.
[19] I. Kovalenko, B. Zdyrko, A. Magasinski, B. Hertzberg, Z. Milicev, R. Burtovyy, I. Luzinov, G. Yushin, *Science* **2011**, *334*, 75.
[20] C. K. Chan, H. Peng, G. Liu, K. McIlwrath, X. F. Zhang, R. A. Huggins, Y. Cui, *Nat. Nanotechnol.* **2008**, *3*, 31.
[21] X. Wang, L. Sun, R. A. Susantyoko, Y. Fan, Q. Zhang, *Nano Energy* **2014**, *8*, 71.
[22] G. G. Eshetu, H. Zhang, X. Judez, H. Adenusi, M. Armand, S. Passerini, E. Figgemeier, *Nat. Commun.* **2021**, *12*, 5459.
[23] B. Dunn, H. Kamath, J.-M. Tarascon, *Science* **2011**, *334*, 928.
[24] P. Poizot, J. Gaubicher, S. Renault, L. Dubois, Y. Liang, Y. Yao, *Chem. Rev.* **2020**, *120*, 6490.
[25] Z. Song, H. Zhou, *Energy Environ. Sci.* **2013**, 2280.
[26] M. Armand, S. Grugeon, H. Vezin, S. Laruelle, P. Ribière, P. Poizot, J. M. Tarascon, *Nat. Mater.* **2009**, *8*, 120.
[27] T. B. Schon, B. T. McAllister, P.-F. Li, D. S. Seferos, *Chem. Soc. Rev.* **2016**, *45*, 6345.
[28] Y. Liang, Z. Tao, J. Chen, *Adv. Energy Mater.* **2012**, *2*, 742.
[29] A. Banerjee, N. Khossossi, W. Luo, R. Ahuja, *J. Mater. Chem. A* **2022**, *10*, 15215.
[30] J. Park, C. W. Lee, S. H. Joo, J. H. Park, C. Hwang, H.-K. Song, Y. S. Park, S. K. Kwak, S. Ahn, S. J. Kang, *J. Mater. Chem. A* **2018**, *6*, 12589.
[31] J. Park, C. W. Lee, J. H. Park, S. H. Joo, S. K. Kwak, S. Ahn, S. J. Kang, *Adv. Sci.* **2018**, *5*, 1801365.
[32] J. Park, S. H. Joo, Y.-J. Kim, J. H. Park, S. K. Kwak, S. Ahn, S. J. Kang, *Adv. Funct. Mater.* **2019**, *29*, 1902888.
[33] J. Park, J. H. Park, M. Yang, S. H. Joo, S. K. Kwak, S. Ahn, S. J. Kang, *Energy Storage Mater.* **2021**, *36*, 123.
[34] K. Eom, M. Kang, J. H. Park, S. H. Joo, J. Park, J. Lee, S. K. Kwak, S. Ahn, S. J. Kang, *J. Mater. Chem. A* **2021**, *9*, 20607.
[35] J. Park, S. H. Joo, M. Kang, J. H. Park, B. Kim, S. K. Kwak, S. Ahn, S. J. Kang, *ACS Energy Lett.* **2022**, *7*, 4142.
[36] J. H. Ha, M. Kang, H. Cha, J. Park, M. Lee, S. H. Joo, S. Ahn, S. J. Kang, *ACS Nano* **2025**, *19*, 2475.
[37] J. Xie, Q. Zhang, *J. Mater. Chem. A* **2016**, *4*, 7091.
[38] S. Ou, C. Liu, R. Yang, W. Fan, Z. Xie, B. Li, T. Meng, C. Zou, D. Shu, Y. Tong, *Energy Storage Mater.* **2024**, *73*, 103814.
[39] M. Niu, L. Dong, J. Yue, Y. Li, Y. Dong, S. Cheng, S. Lv, Y.-H. Zhu, Z. Lei, J.-Y. Liang, S. Xin, C. Yang, Y.-G. Guo, *Angew. Chem., Int. Ed.* **2024**, *63*, 202318663.
[40] X. Gu, Q. Zhang, Q. Chen, Z. Yang, Q. Zhai, Y. Jiao, J. Zuo, H. Duan, P. Zhai, Y. Gong, *Adv. Mater.* **2025**, *37*, 2501448.
[41] J. Zhou, K. Ma, X. Lian, Q. Shi, J. Wang, Z. Chen, L. Guo, Y. Liu, A. Bachmatiuk, J. Sun, R. Yang, J.-H. Choi, M. H. Rümmeli, *Small* **2022**, *18*, 2107460.
[42] J. H. Suh, S. A. Han, S. Y. Yang, J. W. Lee, Y. Shimada, S.-M. Lee, J.-W. Lee, M.-S. Park, J. H. Kim, *Adv. Mater.* **2025**, *37*, 2414117.
[43] R. Yuge, N. Tamura, T. Manako, K. Nakano, K. Nakahara, *J. Power Sources* **2014**, *266*, 471.
[44] Y. Liu, S. Yang, H. Guo, Z. Wang, J. Liu, N. Chen, X. Gong, *Energy Storage Mater.* **2024**, *73*, 103806.
[45] N. Lin, T. Xu, T. Li, Y. Han, Y. Qian, *ACS Appl. Mater. Interfaces* **2017**, *9*, 39318.
[46] T. K. Pham, J. H. Shin, N. C. Karima, Y. S. Jun, S.-K. Jeong, N. Cho, Y.-W. Lee, Y. Cho, S. N. Lim, W. Ahn, *J. Power Sources* **2021**, *506*, 230244.
[47] S. M. Park, T. T. Salunkhe, J. H. Yoo, I. H. Kim, I. T. Kim, *Nanomaterials* **2024**, *14*, 1953.
[48] J. Liu, X. Li, Q. Wang, Y. Kawazoe, P. Jena, *J. Mater. Chem. A* **2018**, *6*, 13816.
[49] H. Zhang, Y. Yang, D. Ren, L. Wang, X. He, *Energy Storage Mater.* **2021**, *36*, 147.
[50] W. Cai, C. Yan, Y.-X. Yao, L. Xu, X.-R. Chen, J.-Q. Huang, Q. Zhang, *Angew. Chem., Int. Ed.* **2021**, *60*, 13007.
[51] Y. Kim, M. Kang, Y. H. Kim, E.-K. Suh, M. Yang, S. Y. Cho, D.-Y. Jeon, J. G. Kim, J. Kim, S. Ahn, *Carbon* **2022**, *200*, 21.
[52] B. Suthar, J. Landesfeind, A. Eldiven, H. A. Gasteiger, *J. Electrochem. Soc.* **2018**, *165*, 2008.
[53] J. A. Steele, E. Solano, D. Hardy, D. Dayton, D. Ladd, K. White, P. Chen, J. Hou, H. Huang, R. A. Saha, L. Wang, F. Gao, J. Hofkens, M. B. J. Roeffaers, D. Chernyshov, M. F. Toney, *Adv. Energy Mater.* **2023**, *13*, 2300760.
[54] J. Park, S. S. Park, Y. S. Won, *Electrochim. Acta* **2013**, *107*, 467.
[55] S. Huang, X. Yao, J. Bai, Z. Huang, X. Liu, *Materials* **2023**, *16*, 541.
[56] Q. Gan, N. Qin, H. Guo, F. Zhang, H. Yuan, W. Luo, Z. Li, Y. Li, L. Lu, Z. Xu, L. Wang, J. Lu, Z. Lu, *ACS Energy Lett.* **2024**, *9*, 1562.
[57] T. Rao, P. Gao, Z. Zhu, S. Wang, L. Ben, Y. Zhu, *Solid State Ionics* **2022**, *376*, 115860.
[58] T. Kim, W. Choi, H.-C. Shin, J.-Y. Choi, J. M. Kim, M.-S. Park, W.-S. Yoon, *J. Electrochem. Sci. Technol* **2020**, *11*, 14.
[59] D. J. Lipomi, R. V. Martinez, G. M. Whitesides, *Angew. Chem., Int. Ed.* **2011**, *50*, 8566.
[60] C. Wang, A. J. Appleby, F. E. Little, *J. Electroanal. Chem.* **2001**, *497*, 33.
[61] D. Jang, S. Suh, H. Yoon, J. Kim, H. Kim, J. Baek, H.-J. Kim, *Appl. Surface Sci. Adv.* **2021**, *6*, 100168.
[62] R. Gao, J. Tang, S. Lin, K. Matsuo, K. Uchida, Y. Matsumoto, L.-C. Qin, *Electrochim. Acta* **2024**, *484*, 143829.
[63] Y. Fang, D. Lu, J. Xie, H. Guo, J. Tian, X. Sun, D. Wang, *Electrochim. Acta* **2025**, *525*, 146075.
[64] K. Xu, X. Li, X. Liu, Y. Yu, X. Zhang, W. Lei, Z. Xie, S. Zhang, Q. Jia, H. Zhang, *Sustain. Mater. Technol.* **2023**, *36*, 00583.